Photocatalytic Properties of Sn-doped TiO2

I.F. Myronyuk[1], V.O. Kotsyubynsky[1], V.M. Boychuk[1], I.M. Mykytyn[1], V.M. Gun'ko[2]

[1] *Vasyl Stefanyk Precarpathian National University, 57 Shevchenko St., 76018 Ivano-Frankivsk, Ukraine*
[2] *Chuiko Institute of Surface Chemistry, Kyiv, Ukraine*

The synthesis of Sn-doped titania nanoparticles (Sn content of 0, 3, 6, and 12 at. %) was carried out using sol-gel chemical route based on the common acid hydrolysis of titanium and tin tetrachlorides. Phase composition, morphology, particle size, pore size distribution and photocatalytic performance of obtained materials were systematically studied by various analytical techniques (XRD, HR-TEM, low-temperature nitrogen adsorption porosimetry, UV-Vis spectroscopy). An increase in the Sn dopant concentration causes a gradual decrease in the relative content of the anatase phase from 100 mol. % for undoped titania to about 3 mol. % for material with maximal doping concentration. Materials with a Sn atomic content of 3 and 6 at. % have the maximum values of the specific surface area (about 280-290 m^2/g) that corresponds to the smallest (approximately 2.5 nm) anatase crystallite. The photocatalytic activity of the synthesized Sn-doped TiO2 nanoparticles was analyzed by the method of methylene blue dye photodegradation in an aqueous solution under UV irradiation. The highest reaction rate constant and maximal methylene blue dye adsorption capacity were obtained for 3 at. % Sn-doped titania with the mixed anatase/rutile composition. The indirect optical transitions are characteristic for all synthesized materials. A decrease in the bandgap energy values with increasing Sn content from 3.21 eV for pure anatase to 2.82 eV for titania doped with 12 at. % of the Sn was observed. The growth in photocatalytic activity for the mixed-phase sample can be considered as a result of the increasing number of surface active centers due to the anatase-rutile phase transition.

Keywords: Titania, Sol-gel, Photocatalysis, Bandgap.

1. INTRODUCTION

Titanium dioxide is the most widely used photocatalyst for last decades due to its high performance, environmental safety and low cost. The main reason of high photocatalytic activity of titania is its electronic structure – the redox potentials for photogenerated in anatase holes and electrons are + 2.53 V and – 0.52 V so these electrons are reducing enough to produce superoxide from oxygen or hydrogen peroxide from water. The main disadvantage of titania as a heterogeneous photocatalyst is a relative wide bandgap: 3.0 eV for rutile (most thermodynamically stable phase of titania), 3.2 eV for anatase and 3.1 eV for brookite (metastable phases of titania), – so pure TiO2 is photoactive under UV light only. The photocatalytic activity of titania can be tuned by the control of phase composition, particle's morphology, and surface properties [1].

Anatase demonstrates respectively higher photocatalytic activity compared to monophase rutile or brookite samples. The main reason of these properties is a beneficial combination of electronic properties - accordingly to some only anatase from all TiO2 forms close to indirect bandgap that corresponds to respectively longer lifetime of photogenerated electrons and holes with lightest average effective mass [2]. From another hand, there are a lot of data on direct type of anatase optical bandgap [3]. Other reasons for better photoactivity of anatase are more effective charge transport and respectively wider bandgap that allows to raise the valence band maxima to higher energy levels relative to redox potentials of adsorbed molecules [4]. The titania photocatalytic performance increasing due to absorption enhancement in the visible region is possible as a result of TiO2 doping with metal and non-metal species [5] or using the reduced forms of titania (TiO$_x$) photocatalysts [6].

There are a lot of results on metal-doped titania photocatalysts with iron [7], chromium [8], nickel [9], tin [10], etc. In most cases, the shift of UV-Vis absorbance for the metal-doped titania powders was observed to longer wavelengths in the range of 400-600 nm. At the same time, an increase in the absorption of metal-doped titania in some cases leaving unaffected intrinsic bandgap [11]. The method of metal-doped titania preparation is important. Cr- or Fe-doped TiO2 prepared by the magnetron sputtering demonstrate the band gap narrowing while the titania samples doped with the same concentration of Cr and Fe ions using sol-gel are characterized only impurity energy levels presence into the bandgap [12]. The aim of the present work is to test the effects of structural and morphological properties of sol-gel prepared Sn-doped titania samples with different dopant concentration on the photocatalytic activity in reaction with methylene blue (MB).

2. EXPERIMENT

Undoped and Sn-doped titania powders were synthesized using sol-gel method. The initial sol was prepared by hydrolysis of titanium tetrachloride as a titania precursor and tin tetrachloride as a source of Sn dopant [13, 14]. Undoped TiO2 was synthesized as a control sample. TiCl4 (Merck, 99.9 %; specific density 1.73 g/cm^3 at 20 °C) and hydrochloric acid (36.0 % aqueous solution) were mixed at the temperature 0-5 °C with gaseous hydrogen chloride evaporation and the formation of titanium oxychloride TiCl3OH. The several different molar concentrations of SnCl4 were realized in the reaction mixture at the hydrolysis to reach Sn at. % values of 3, 6, and 12, respectively, in the Sn-doped TiO2. Sodium hydrocarbonate aqueous solution was added dropwise to sol of up to pH = 5.0-5.5 under vigorous stirring with gel formation. The sus-

pension of nanoparticles was kept at 80 °C for 48 h with the next multiplied washing procedure. Sn-doped TiO₂ samples were dried at 120 °C for 2 h. The samples were labeled as 0Sn-TiO₂, 3Sn-TiO₂, 6Sn-TiO₂, and 12Sn-TiO₂, respectively. Structure of the obtained powders were characterized by X-ray diffraction (XRD, CuK$_a$ radiation, NiK$_\beta$-filter) using full pattern Rietveld refinement (FullProf Suite Program). The models of anatase and rutile structures were based on ICSD #92363 and ICSD #24780, respectively. The morphological properties of the samples were investigated using high-resolution transmission electron microscopy (HRTEM, 200 kV, JEM-2100F microscope). The specific surface area was measured by the BET method (low temperature nitrogen adsorption/desorption at 77 K, Quantachrome NOVA 2200e device). All measurements were realized after sample degassing at 160 °C for 24 h. The pore size distribution functions were calculated using NLDFT approach (cylindrical pore model).

The photocatalytic activity of the Sn-doped TiO₂ samples was investigated on the methylene blue (MB) decolorization in an aqueous solution (mass concentration of 0.01 g/l) under the illumination of soft UV light (27 W, predominantly wavelength 365 nm). Dry titania powder (mass concentration 0.1 g/l) after continuous grinding was added into an aqueous solution of MB. The total volume of reaction media was 50 ml, interface area – 30 cm², the irradiation was under magnetic stirring. The reaction time ranged from 0 to 50 min, the concentration measurements were performed each 10 min. The titania catalyst and solution were separated with a centrifuge. The changes of reaction media absorbance were measured with UV/Vis spectrophotometer Ulab 108UV, China.

3. RESULTS AND DISCUSSION

Fig. 1 shows the XRD diffraction pattern of the non-doped TiO₂. All observed reflexes correspond to the anatase phase. The evolution of XRD patterns of Sn-doped titania is caused by anatase-rutile transformation with increasing Sn concentration.

The phase composition of the samples during the anatase – rutile transition was determined from anatase (101) and rutile (110) reflections intensities (I_A and I_R, respectively).

The weight fraction of anatase was calculated according to following equation: $X_A = \dfrac{1.26R}{1+1.26R} \times 100\%$,

were $R = \dfrac{I_A}{I_R}$. For the 3Sn-TiO₂ sample, anatase content is 66.2 ± 2.2 wt.%, but for 6Sn-TiO₂ and 12Sn-TiO₂ materials rutile phase is dominating (anatase contents are 42.8 ± 2.3 and 2.9 ± 1.2 wt. %, respectively) (Fig. 2).

A main advantage of the SPP method is less importance of data on reflections at high angles with respectively lower precision. Accordingly to the SSP method, the broadening of reflection peaks caused by coherent scattering regions (CSR) size changes is described by a Lorentzian function when strain-induced profile broadening by a Gaussian function. The SSP approach to analyze XRD pattern data was realized using the relation:

$$\left(d_{hkl}\beta_{hkl}\cos\theta/\lambda\right)^2 = \frac{K}{D}\left(d_{hkl}^2\beta_{hkl}\cos\theta/\lambda\right)+\left(2\varepsilon\right)^2,$$

where D is the CSR size, λ is the X ray wavelength (0.154056 nm for CuK$_a$ radiation), β is the (hkl) peak width at a half-maximum intensity and θ is the peak position, K is a constant depending on the crystallite shape and for spherical particles $K = 0.75$, ε is the relative strain module.
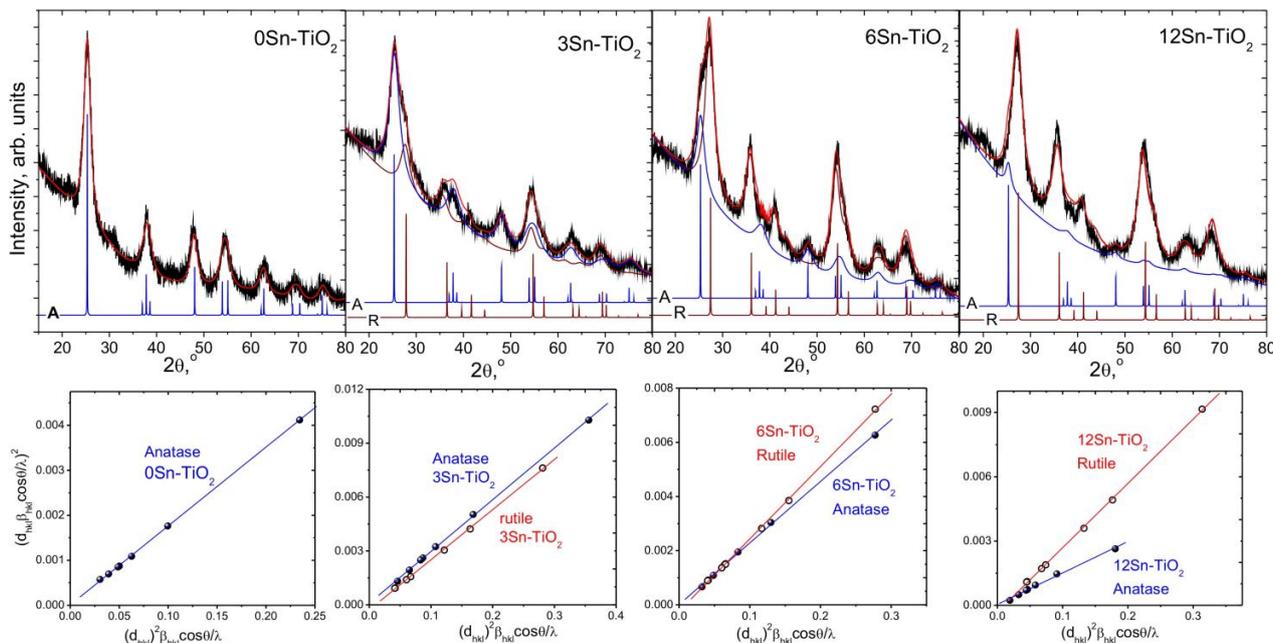

Fig. 1 – The XRD pattern of Sn-doped TiO₂ (a) and corresponding SSP plots for anatase and rutile phases (CSR size is calculated from the slope of the linear fitted data and the root of y-intercept gives the strains

The plotting of $(d_{hkl}\beta_{hkl}\cos\theta/\lambda)^2$ values as a function of $d^2_{hkl}\beta_{hkl}\cos\theta/\lambda$ allows us to determine the average CSR size from the slope of the linearly fitted data and the root of the *y*-intercept gives the doubled strain. The non-linear change of anatase phase CSR sizes with local minimum at Sn content of 6 at. % was observed while the rutile particle sizes are independent of the doping conditions (Fig. 2).

The BET surface area of the samples depends on the amount of Sn. The largest surface area values (281 and 290 m²g⁻¹) correspond to minimal values of particle sizes (3Sn-TiO₂ and 6Sn-TiO₂ samples, respectively) (see Fig. 2). In terms of shape, adsorption isotherm of pure titania (Fig. 3a) is close to type I (Langmuir) with small hysteresis that corresponds to dominance of micropores and the adsorption limited by the accessible pore volume [15]. All Sn-containing samples have type V isotherms (Fig. 3a) that indicate the presence of poorly developed micropore, large numbers of mesopores and macropore absence. The hysteresis loop could be classified as type D which is associated with bottle-neck pores [16]. In this case, the hysteresis is a result of desorption delay from the pores with narrow neck while the adsorption occurs more readily. DFT calculation of pore-size distribution confirms microporous structure of undoped titania and mesopores dominance of Sn-doped titania samples (Fig. 3b).
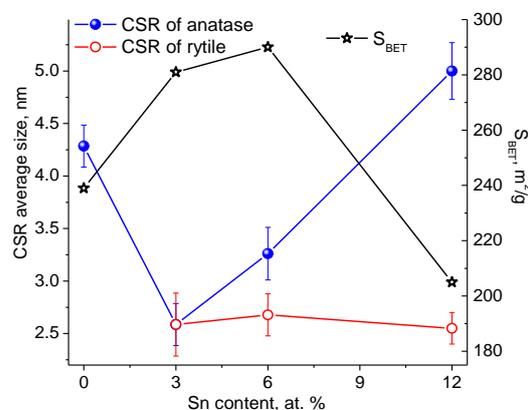

Fig. 2 – The average particle size of anatase and rutile phases of Sn-doped TiO₂ and BET specific surface area as a function of dopant content
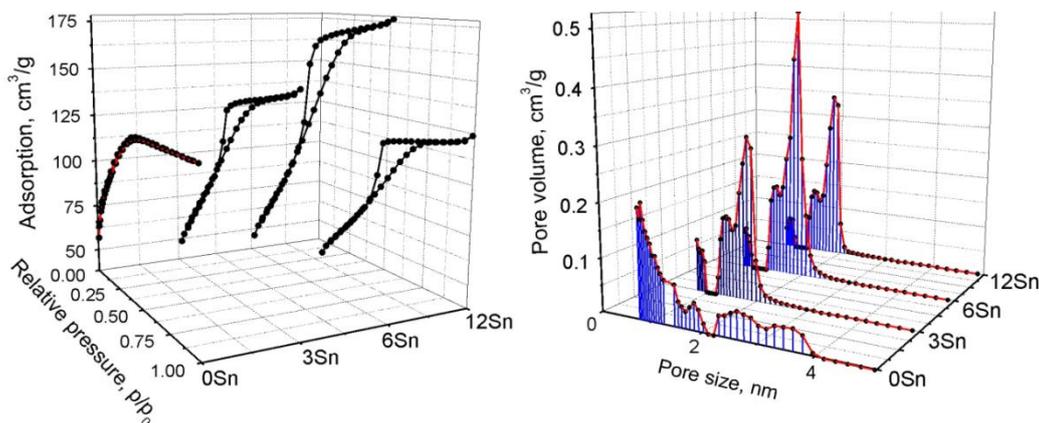

Fig. 3 – Absorption-desorption isotherms at 77 K (a) and pore-size distributions (DFT approach) for prepared Sn-TiO₂ samples (b)
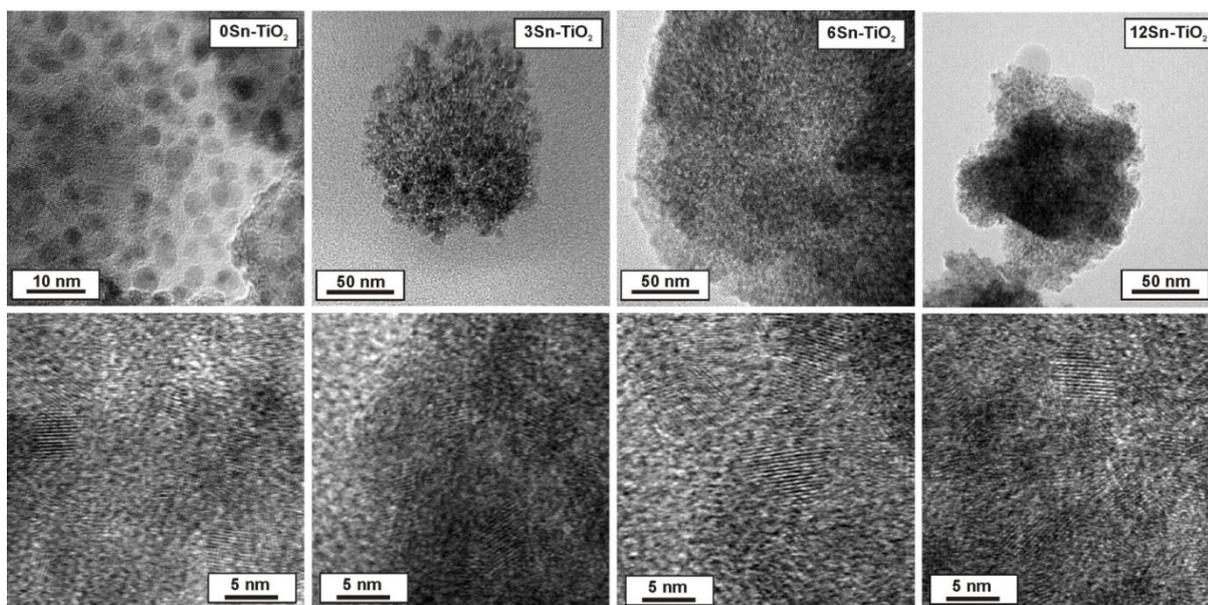

Fig. 4 – HRTEM images of Sn-TiO₂ samples

The TEM image (Fig. 4a) of 0Sn-TiO₂ sample depicts well defined spherical nanocrystals with the average size of about 4.5-5.5 nm that corresponds to XRD data and confirms the assumption about the close size of CRS and separate TiO₂ particles. Sn content increasing causes the agglomeration of particle with the formation of bottle-neck type mesopores (Fig. 4b-d).

It is obvious that the samples are consist of very good crystallized areas of nanosized titania. The interlayer spacing $d = 0.35$ nm of all samples corresponding to the (101) plane of anatase (Fig. 4b). As compare to undoped anatase, the fringes of doped anatase lattice are expanded and showed considerable waviness. These dislocations were possibly attributed to electric stress, which may originate from interstitial ions doping [17].

UV-Vis absorbance spectra allow one to estimate the band gap energy of the samples using the Tauc plot (Fig. 5) accordingly to equation is given as $(\alpha h\nu) = A(h\nu - E_g)^n$, where α is an absorption coefficient, A is a constant, E_g is bandgap energy and n is an exponent that determines the transition type ($n = 2$ and $n = 0.5$ for the direct and indirect types of optical transition, respectively). Better results were obtained at $n = 0.5$ that indicates the indirect transitions dominating. The band gap energy of pure TiO₂ obtained from Tauc plot is about 3.21 eV. The increasing of Sn content caused E_g decreasing from 3.09 to 2.99 and 2.82 eV as

the Sn content increased from 3 to 6 and 12 at. %, according to Fig. 5 (the inset). The decrease in bandgap energy plays a crucial role in the photocatalytic activity under natural sunlight.

The adsorption ability of MB dye by obtained samples was tested at conditions similar to the testing of its photocatalytic ability but in the dark (Fig. 6). The obtained results (see absorbance spectra below) correspond to the low-temperature nitrogen absorption data about the morphology of Sn-doped titania.
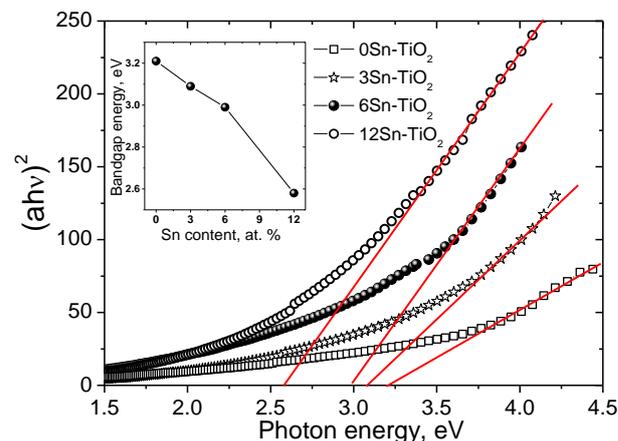

Fig. 5 – Tauc plot of Sn-TiO₂ samples and change in the bandgap energy as a function of Sn ion content (the inset)
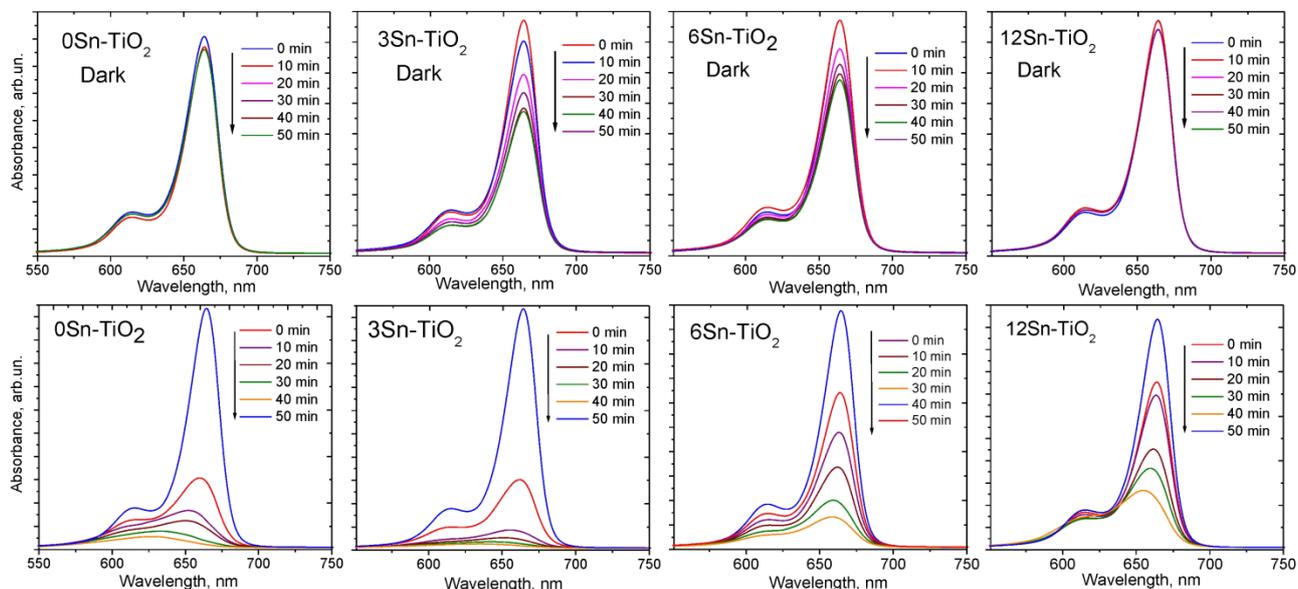

Fig. 6 – Time evolution of the absorbance spectra of MB dye and Sn-doped TiO₂ colloidal solutions in the dark and under irradiation

The best absorbance performance was observed for 3Sn-TiO₂ and 6Sn-TiO₂ samples with the highest value of the specific surface area. Thus, for Sn-doped titania, there are several electronic factors affecting both electronic structure (e.g., E_g) and adsorption interactions with charged molecules such as MB due to changes in charge distribution [18]. This adsorption influences subsequent photodegradation of bound MB.

The degradation of MB dye molecules in aqueous solution under UV light irradiations was realized to

test the photocatalytic performance of Sn-doped titania with different Sn contents. The intensity of MB characteristic absorbance ($\lambda_{max} = 667$ nm) continuously decreases without shifting the maximum wavelength with increasing irradiation time that corresponds to gradual degradation of MB molecules (Fig. 6). The kinetic plots of MB photodegradation on Sn-TiO₂ particles are presented in Fig. 7.

Nearly linear type of these dependencies indicates pseudo-first order rate of MB photocatalytic degrada-

tion [19]. The maximal value of the rate constant is observed for 3Sn-TiO₂ sample (0.088 min^{-1}) when this parameter
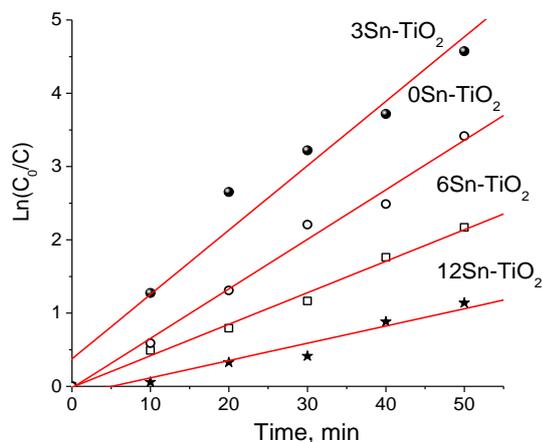

Fig. 7 – The kinetics of MB photocatalytic degradation on Sn-TiO₂ particles

for undoped titania is respectively smaller (0.067 min^{-1}) (Fig. 3b). The next increase of Sn concentration causes the rate constant decreasing (0.046 and 0.024 min^{-1} for Sn contents of 6 and 12 at. %, respectively). These results reflect the balance of several factors: the decreasing of anatase content, the changes of specific surface area values and the bandgap narrowing.

4. CONCLUSIONS

Sn-doped titania nanoparticles with different Sn content were successfully prepared using chloric acid hydrolysis of TiCl₄ and SnCl₄ as precursors. Sn content increasing in the range of 0-12 at. % causes a decrease in anatase phase content from 100 to about 3 wt. %. The maximal values of the specific surface area were observed for Sn content of 3 and 6 at. % that reflects the anatase-rutile phase transition and a decrease in the average size of anatase crystallites. All Sn-doped samples have a mesoporous structure, but undoped titania is mainly microporous. Predominant orientation of anatase crystals along the (101) planes was confirmed by HR-TEM images. The optical bandgap narrowing from 3.2 eV for pure titania to 2.82 eV for the sample doped with 12 at. % Sn was observed. The best photocatalytic performance for MB dye degradation under UV irradiation is for Sn-doped (3 at. %) TiO₂ with an anatase content of about 66 wt. % and the smallest (2.6 nm) average size of crystallites. Differences in the photocatalytic activity of Sn-doped titania samples simultaneously depend on the phase composition, surface area, average particle size, and changes in the bandgap.

REFERENCES

1. A.L. Linsebigler, G.Lu, J.T. Yates, _Chem. Rev._ **95**, 735 (1995).
2. J. Zhang, P. Zhou, J. Liu, J. Yu, _Phys. Chem. Chem. Phys._ **16**, 20382 (2014).
3. A. Kadam, R. Dhabbe, D.S. Shin, K. Garadkar, J. Park, _Ceram. Int._ **43**, 5164 (2017).
4. M. Batzill, _Energy Environ. Sci._ **4**, 3275 (2011).
5. A. Zaleska, _Recent Patents on Engineering_ **2**, 157 (2008).
6. A. Naldoni, M. Altomare, G. Zoppellaro, N. Liu, S. Kment, R. Zboril, P. Schmuki, _ACS Catalysis_ **9**, 345 (2018).
7. D.H. Kim, H.S. Hong, S.J. Kim, J.S. Song, K.S. Lee, _J. Alloy. Compd._ **375**, 259 (2004).
8. Y.H. Peng, G. F. Huang, W.Q. Huang, _Adv. Powder Technol._ **23**, 8 (2012).
9. D. Hyun Kim, K. Sub Lee, Y.S. Kim, Y.C. Chung, S.J. Kim, _J. Am. Ceram. Soc._ **89**, 515 (2006).
10. Y.F. Tu, S.Y. Huang, J.P. Sang, X.W. Zou, _J. Alloy. Compd._ **482**, 382 (2009).
11. E. Arpac, F. Sayılkan, M. Asiltürk, P. Tatar, N. Kiraz, H. Sayılkan, _J. Hazard. Mater._ **140**, 69 (2007).
12. R. Dholam, N. Patel, M. Adami, A. Miotello, _Int. J. Hydrogen. Energ._ **34**, 5337 (2009).
13. V.O. Kotsyubynsky, I.F. Myronyuk, L.I. Myronyuk, V.L. Chelyadyn, M.H. Mizilevska, A.B. Hrubiak, F.M. Nizamutdinov, _Materialwiss. Werkst._ **47**, 288 (2016).
14. V.O. Kotsyubynsky, I.F. Myronyuk, V.L. Chelyadyn, A.B. Hrubiak, V.V. Moklyak, S.V. Fedorchenko, _Nanoscale. Res. Lett._ **12**, 369 (2017).
15. K.S.W. Sing, D.H. Everett, R.A.W. Haul, I. Moscou, R.A. Pierotti, J. Rouquerol, T. Siemieniewska, _Pure. Appl. Chem._ **57**, 603 (1985).
16. A.E. Machado, K.A. Borges, T.A. Silva, L.M. Santos, M.F. Borges, W.A. Machado, A.O. Patrocíni, _Sol. Radiation Appl._ **5**, 87 (2015).
17. V. Štengl, S. Bakardjieva, N. Murafa, _Mater. Chem. Phys._ **114**, 217 (2009).
18. M.J. Frisch, G.W. Trucks, H.B. Schlegel, G.E. Scuseria, M.A. Robb, J.R. Cheeseman et al., _Inc. Wallingford CT_ (2013).
19. X.H. Wang, J.G. Li, H. Kamiyama, Y. Moriyoshi, T. Ishigaki, _J. Phys. Chem. B._ **110**, 6804 (2006).